

REPORT DOCUMENTATION PAGE			Form Approved OMB NO. 0704-0188		
<p>The public reporting burden for this collection of information is estimated to average 1 hour per response, including the time for reviewing instructions, searching existing data sources, gathering and maintaining the data needed, and completing and reviewing the collection of information. Send comments regarding this burden estimate or any other aspect of this collection of information, including suggestions for reducing this burden, to Washington Headquarters Services, Directorate for Information Operations and Reports, 1215 Jefferson Davis Highway, Suite 1204, Arlington VA, 22202-4302. Respondents should be aware that notwithstanding any other provision of law, no person shall be subject to any penalty for failing to comply with a collection of information if it does not display a currently valid OMB control number.</p> <p>PLEASE DO NOT RETURN YOUR FORM TO THE ABOVE ADDRESS.</p>					
1. REPORT DATE (DD-MM-YYYY) 19-10-2012		2. REPORT TYPE Final Report		3. DATES COVERED (From - To) 1-Jul-2008 - 30-Jun-2011	
4. TITLE AND SUBTITLE FINALPROJECT REPORT: W911NF-08-1-0196 “EXPLORING NOVEL FORMS OF SUPERCONDUCTIVITY....”			5a. CONTRACT NUMBER W911NF-08-1-0186		
			5b. GRANT NUMBER		
			5c. PROGRAM ELEMENT NUMBER 611102		
6. AUTHORS Jak Tchakhalian			5d. PROJECT NUMBER		
			5e. TASK NUMBER		
			5f. WORK UNIT NUMBER		
7. PERFORMING ORGANIZATION NAMES AND ADDRESSES University of Arkansas University of Arkansas 210 Administration Building Fayetteville, AR 72701 -1201			8. PERFORMING ORGANIZATION REPORT NUMBER		
9. SPONSORING/MONITORING AGENCY NAME(S) AND ADDRESS(ES) U.S. Army Research Office P.O. Box 12211 Research Triangle Park, NC 27709-2211			10. SPONSOR/MONITOR'S ACRONYM(S) ARO		
			11. SPONSOR/MONITOR'S REPORT NUMBER(S) 54374-PH.3		
12. DISTRIBUTION AVAILABILITY STATEMENT Approved for Public Release; Distribution Unlimited					
13. SUPPLEMENTARY NOTES The views, opinions and/or findings contained in this report are those of the author(s) and should not be construed as an official Department of the Army position, policy or decision, unless so designated by other documentation.					
14. ABSTRACT Novel growth method for unit cell thin superlattices of complex oxides is discovered. Novel class nickelate based heterostructures is created and studied in details by conventional transport methods, IR optics and resonant soft X-ray spectroscopy. The results demonstrate the profound ability of the interface to promote a new electronic and magnetic ground state not attainable in the bulk constituent layers.					
15. SUBJECT TERMS artificial oxide heterostructures					
16. SECURITY CLASSIFICATION OF:			17. LIMITATION OF ABSTRACT UU	15. NUMBER OF PAGES	19a. NAME OF RESPONSIBLE PERSON Jak Tchakhalian
a. REPORT UU	b. ABSTRACT UU	c. THIS PAGE UU			19b. TELEPHONE NUMBER 479-575-4313

### Report Title

FINALPROJECT REPORT: W911NF-08-1-0196 “EXPLORING NOVEL FORMS OF SUPERCONDUCTIVITY....”

### ABSTRACT

Novel growth method for unit cell thin superlattices of complex oxides is discovered. Novel class nickelate based heterostructures is created and studied in details by conventional transport methods, IR optics and resonant soft X-ray spectroscopy. The results demonstrates the profound ability of the interface to promote a new electronic and magnetic ground state not attainable in the bulk constituent layers.

---

**Enter List of papers submitted or published that acknowledge ARO support from the start of the project to the date of this printing. List the papers, including journal references, in the following categories:**

**(a) Papers published in peer-reviewed journals (N/A for none)**

Received

Paper

**TOTAL:**

**Number of Papers published in peer-reviewed journals:**

---

**(b) Papers published in non-peer-reviewed journals (N/A for none)**

Received

Paper

**TOTAL:**

**Number of Papers published in non peer-reviewed journals:**

---

**(c) Presentations**

**Number of Presentations:** 24.00

---

**Non Peer-Reviewed Conference Proceeding publications (other than abstracts):**

Received

Paper

TOTAL:

Number of Non Peer-Reviewed Conference Proceeding publications (other than abstracts):

---

Peer-Reviewed Conference Proceeding publications (other than abstracts):

Received

Paper

TOTAL:

Number of Peer-Reviewed Conference Proceeding publications (other than abstracts):

---

(d) Manuscripts

Received

Paper

12/24/2009

1.00

Jian Liu, M. Kareev, S. Prosandeev, B. Gray, P. Ryan, J.W. Freeland, J. Chakhalian. Effect of polar discontinuity on the growth of LaNiO3/LaAlO3 superlattices, (12 2009)

TOTAL: 1

Number of Manuscripts:

---

Books

Received

Paper

TOTAL:

## Patents Submitted

---

## Patents Awarded

---

## Awards

2010- Charles Scharlau Endowed Chair

Advanced Photon Source Award for best publication - 2012

Advanced Light Source Award for Thesis work in residence - 2010-2012

Olshanski Award by American Physics Society- 2012

---

## Graduate Students

<u>NAME</u>	<u>PERCENT SUPPORTED</u>	Discipline
Jian Jiu	1.00	
Benjamin Gray	1.00	
<b>FTE Equivalent:</b>	<b>2.00</b>	
<b>Total Number:</b>	<b>2</b>	

---

## Names of Post Doctorates

<u>NAME</u>	<u>PERCENT SUPPORTED</u>
Michal Kareev	1.00
<b>FTE Equivalent:</b>	<b>1.00</b>
<b>Total Number:</b>	<b>1</b>

---

## Names of Faculty Supported

<u>NAME</u>	<u>PERCENT SUPPORTED</u>	National Academy Member
Jak Tchakhalian	0.50	
<b>FTE Equivalent:</b>	<b>0.50</b>	
<b>Total Number:</b>	<b>1</b>	

---

## Names of Under Graduate students supported

<u>NAME</u>	<u>PERCENT SUPPORTED</u>	Discipline
Derek Maiers	1.00	Condensed Matter Physics
<b>FTE Equivalent:</b>	<b>1.00</b>	
<b>Total Number:</b>	<b>1</b>	

### Student Metrics

This section only applies to graduating undergraduates supported by this agreement in this reporting period

The number of undergraduates funded by this agreement who graduated during this period: ..... 3.00

The number of undergraduates funded by this agreement who graduated during this period with a degree in science, mathematics, engineering, or technology fields:..... 3.00

The number of undergraduates funded by your agreement who graduated during this period and will continue to pursue a graduate or Ph.D. degree in science, mathematics, engineering, or technology fields:..... 3.00

Number of graduating undergraduates who achieved a 3.5 GPA to 4.0 (4.0 max scale): ..... 3.00

Number of graduating undergraduates funded by a DoD funded Center of Excellence grant for Education, Research and Engineering: ..... 0.00

The number of undergraduates funded by your agreement who graduated during this period and intend to work for the Department of Defense ..... 1.00

The number of undergraduates funded by your agreement who graduated during this period and will receive scholarships or fellowships for further studies in science, mathematics, engineering or technology fields: ..... 3.00

### Names of Personnel receiving masters degrees

NAME

Total Number:

### Names of personnel receiving PhDs

NAME

Jian Liu

Total Number:

1

### Names of other research staff

NAME

PERCENT SUPPORTED

FTE Equivalent:

Total Number:

### Sub Contractors (DD882)

### Inventions (DD882)

**Scientific Progress**

**Technology Transfer**

“EXPLORING NOVEL FORMS OF SUPERCONDUCTIVITY...”

## 1. NEW GROWTH MODE

First we focused on developing a growth mode that is capable of producing a single unit cell thin superlattices of  $\text{LaNiO}_3/\text{LaAlO}_3$  (LNO/LAO thereafter). High-quality epitaxial LNO ultra-thin films (10-15uc) were grown on STO (001) and LAO (001) single crystal substrates by pulsed laser deposition (PLD) with in-situ monitoring by Reflection High Energy Electron Diffraction (RHEED). Due to the lattice mismatch, NNO (3.80Å) is subjected to a tensile strain of 2.6 % on STO (3.90Å), whereas a compressive strain of -0.3 % is applied on LAO (3.79Å). The used LAO substrates had mixed terminations as received, while the STO substrates were prepared by our recently developed chemical wet-etch procedure (Arkansas treatment) to attain

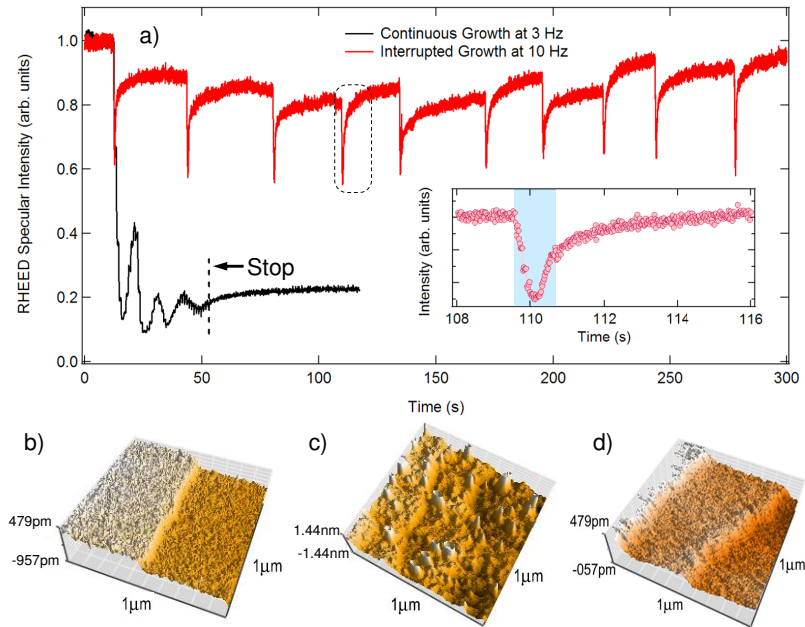


**Figure:** (a) A representative RHEED specular intensity evolution during the continuous slow growth and the interrupted growth with fast laser ablation. Inset: the intensity oscillation during the “laser-on” period (highlighted) of the interrupted growth. AFM scans on the surface of a  $\text{TiO}_2$ -terminated  $\text{SrTiO}_3$  substrate before the growth (b), after the continuous slow growth (c) and the interrupted growth (d).

an atomically flat  $\text{TiO}_2$ -terminated surface with a minimal number of surface bound electronic defects. The growth temperature was in the range of 670-700 C, while the oxygen partial pressure was maintained at 100-120 mTorr. After deposition, to maintain the proper oxygen content, samples were post annealed for 30 minutes and cooled down to room temperature in 1 atmosphere of ultra-pure oxygen.

To maintain the perfect epitaxy, LBL growth is achieved by the interrupted deposition, which requires a rapid laser ablation cycle (up to 30Hz) followed by a prolong time-delay between two successive unit cells. Figure 1(a) and Fig. 2 shows a representative time-dependent RHEED specular intensity (RSI), where the full recovery of RSI, characteristic of the perfect LBL growth, can be seen after each unit-cell layer. Smooth surface morphology is also evident from the well-defined spots of the (00) specular and (01) and (0-1) off-specular reflections with streaks in the resulting RHEED pattern. AFM imaging showed that the sample surface is atomically flat with preserved vicinal steps and typical surface roughness < 80 pm. AFM imaging showed that the sample surface is atomically flat with preserved vicinal steps and typical surface roughness < 80 pm.

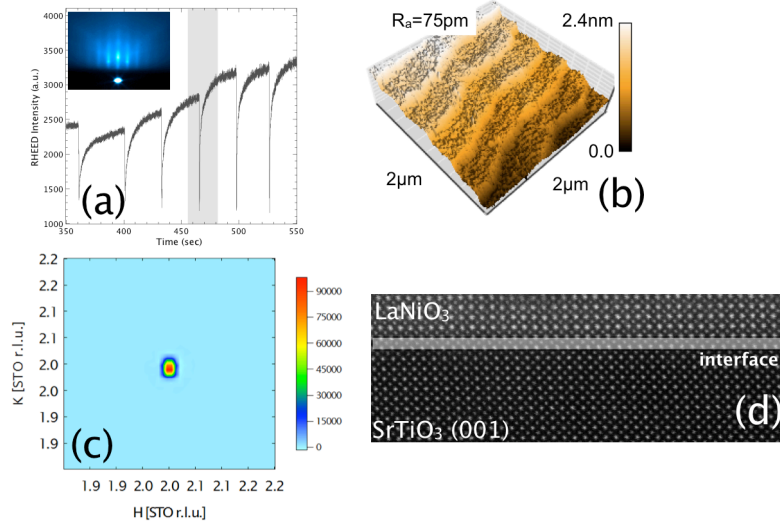


**Figure 2.** Surface morphology and structural characterization of the LNO films. (a) Time-dependent RHEED specular intensity (RSI), where the full recovery of RSI, characteristic of the perfect layer-by-layer (LBL) growth, is observed after each unit-cell layer [indicated by the shaded (grey) area]. Smooth surface morphology is evident from the well-defined spots of the specular and off-specular reflections with a characteristic to quality surface streaks pattern shown in inset. (b) AFM imaging confirms that the sample surface is atomically flat with well-preserved vicinal steps and typical surface roughness <80 pm. (c) A reciprocal space map around (222) reflection of 10 u.c. LNO film grown on STO. A position of the reflection is in perfect registry with the substrate. The absence of diffuse intensity around the peak testifies for the full epitaxy. (d) High resolution TEM image at the film-substrate interface (shaded) also support excellent sample epitaxy.

To elaborate the role of the laser frequency  $f$  during the growth of each unit-cell layer, Fig. 3 shows a schematic of the evolution of the growth dynamics. The nucleation and crystallization in pulsed laser deposition (PLD) are primarily governed by two time scales; one is the length of the "flux-on" period  $t_F$  during which the dense plasma plume typically enforces high supersaturation and nucleation of small islands on the order of one structural unit, while the other is the "relaxation" period  $t_R$  where the absorbed atoms and small islands reach stabler state by diffusing on the surface to form larger islands or migrate to the edges of larger islands.  $t_F$  is relatively short on the scale of  $10^{-4}$  to  $10^{-3}$  s. In contrast,  $t_R$  is about  $10^{-2}$  to  $10^{-1}$  s and much longer. When  $t_R \ll 1/f$ , the small islands always migrate and reach a steady state before the material is delivered again by the next pulse (see Fig. 3(a)). In this case, the LBL growth relies



on the condition that the absorbed atoms have enough mobility to find and fill the voids of the incomplete growing layer. Otherwise, the growth will transform into a 3D island fashion due to stacking of several incomplete layers at the growth front. In contrast, when  $t_R \sim 1/f$ , due to the transitional kinetics imposed by the rapid laser pulsing, the concentration of the small nucleating islands does not fully decay between two consecutive pulses (see Fig. 3(b)). In this case, the growing layer is formed by homogeneous coalescence of small islands instead of isolated large islands, reflected in the better recovery of the RHEED specular intensity. If one is able to decrease  $1/f$  to the order of  $t_F$ , the system will see only an average flux of vapor, and the growth will fall into a continuous MBE- like regime (see Fig. 3(c)). Finally, since there are fewer and fewer voids as the layer coverage improves, some atoms may remain on the surface. In this case, an interruption on the laser ablation can be introduced to delay the delivery of the next layer so as to wait for the layer completion. This corresponds to the slow recovery of the RHEED specular intensity in the "laser-off" period.

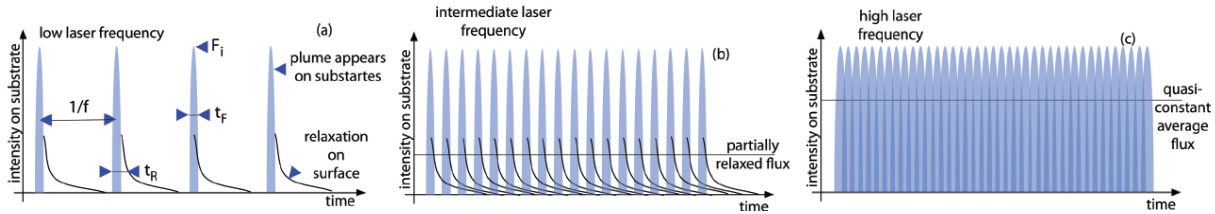


**Figure 3:** Timing diagram showing the modulated flux and relaxation of the island density. During the low-frequency pulsed growth (a), the physical vapor is delivered to the substrate surface where it is relaxed. After increasing the pulse rate (b), the relaxation process becomes more and more delayed. As the frequency (c) reaches the quasi-constant state with average flux, the large degree of supersaturation overcomes the nucleation barrier resulting in the rapid nucleation from the supercritical vapor.

## 2. EFFECT OF POLAR MISMATCH

Recently, the problem of polar interfaces has been drawing enormous attention for building interface- controlled devices, since a polar crystal structure grown on a non-polar substrate would be unstable due to the depolarizing fields. An example is showed in Fig. 4(a) where two perovskites (e.g. LAO and STO) with different charge structures, such as  $A^{3+}B^{3+}O^{2-}$  and  $A^{2+}B^{4+}O^{2-}$ , are interfaced together. The  $+1-1-+1-1$  alternating stacking sequence on the LAO side would resulting in a diverging electrostatic potential or a diverging electric dipole moment, as the LAO slab becomes thicker and thicker. To avoid this unstable divergence, some mechanism must set in to compensate the potential jump by forcing electronic, structural or chemical (non-stoichiometry) changes. In particular, the active work on this LAO/STO system has suggested an electron transfer to the interfacial  $TiO_2$  that decreases Ti valence by 0.5 at the expense of 0.5e charge in the terminating atomic plane (see Fig. 4(b)). This mechanism has been intensively discussed to account for the observed 2D electron gas at the LAO/STO interface, although additional effects such as alloying and ionic displacement have been suggested at the interface.

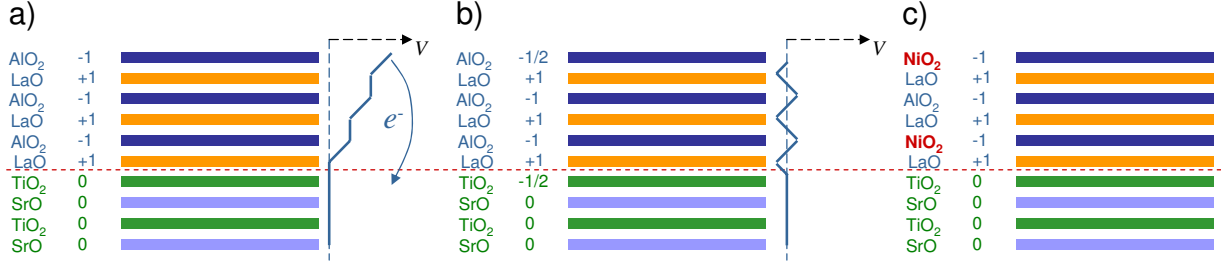


**Figure 4:** Cartoon pictures of polar interfaces of LAO/STO before charge transfer (a), after charge transfer (b), and with some of the LAO layers replaced by LNO in a SL structure (c).  $V$  denotes the electron potential.

A simple fundamental question one can ask is that what if some of the ions at the LAO side are replaced by elements that have multiple valence states. More interestingly, to test the charge-transfer mechanism, we may replace some the LAO layers with LNO (see Fig. 4(c)) where Ni is then supposedly converted from 3+ toward 4+ valence state by giving up electrons. In this section, we will show that, instead of  $\text{Ni}^{4+}$ , an unusual valence state of  $\text{Ni}^{2+}$  is observed in ultra-thin LNO/LAO SLs grown on non-polar (or weakly polar) (001)  $\text{TiO}_2$ -terminated STO substrates. This is in marked contrast to identical SLs grown on polar LAO, which always exhibit the 3+ valence of the bulk-like LNO. To clarify the origin of these phenomena, we have tracked the changes of the Ni valence as a function of the SL thickness and developed an experimental procedure to monitor and control the electronic state of a transition metal ion.

### 3. NOVEL ELECTRONIC PROPERTIES

To get insight into the electronic structure, we carried out detailed soft x-ray absorption spectroscopic measurement, which is particularly useful in probing layers buried within SLs due to the local and element-specific characters. Spectra were acquired in the bulk-sensitive fluorescence yield mode at the Ni L-edge at the 4ID-C beamline of the Advanced Photon Source. The normalized spectra taken at 300 K are shown in Fig. 5. The main peaks' energies and the line shape are similar to the bulk data of  $\text{ReNiO}_3$ , indicative of a  $\text{Ni}^{3+}$  valence state with the 3d<sup>7</sup> low-spin configuration. On the other hand, as  $n$  decreases, the splitting of the double peaks (highlighted in green) at the L3-edge becomes more pronounced, especially from  $n = 10$  to 5. The corresponding trend at the L2-edge emerges as a weak shoulder at about 870.5 eV. Notice that this multiplet splitting is absent in bulk LNO, but reminiscent of the evolution as entering the charge-ordered insulating state in bulk  $\text{ReNiO}_3$ . The emergence of this multiplet splitting in the SLs even with a relatively thick LNO layer ( $n = 10$ ) denotes enhanced localization and hints at a MIT and a latent tendency to charge ordering.

X-ray linear dichroism (XLD) ( $I_{\text{Elab}} - I_{\text{Elc}}$ ) was then measured to acquire the  $e_g$  orbital occupation. Spectral weight transfer in XLD shown in Fig 5 between the main peak and the low-energy multiplet is indicated by the opposite signs, implying the Oh symmetry of the charge distribution is reduced likely to D4h. The main peak's negative XLD signifies more holes populate the  $dz^2$  orbital, resulting from tensile strain and interfacing with LAO. As  $n$  increases, the XLD is rapidly suppressed, and becomes practically zero for  $n = 10$ . The origin for this can be twofold. First, at large thickness, the inherent orbital-lattice interaction of LNO tends to preserve the  $e_g$  degeneracy in response to tensile strain. Second, in a localized-itinerant crossover, such as Mott transition, the kinetic energy gain favors putting electrons in orbitals that participate in band formation as in manganites. In our case, that is the  $dz^2$  orbital with increasing  $n$ .

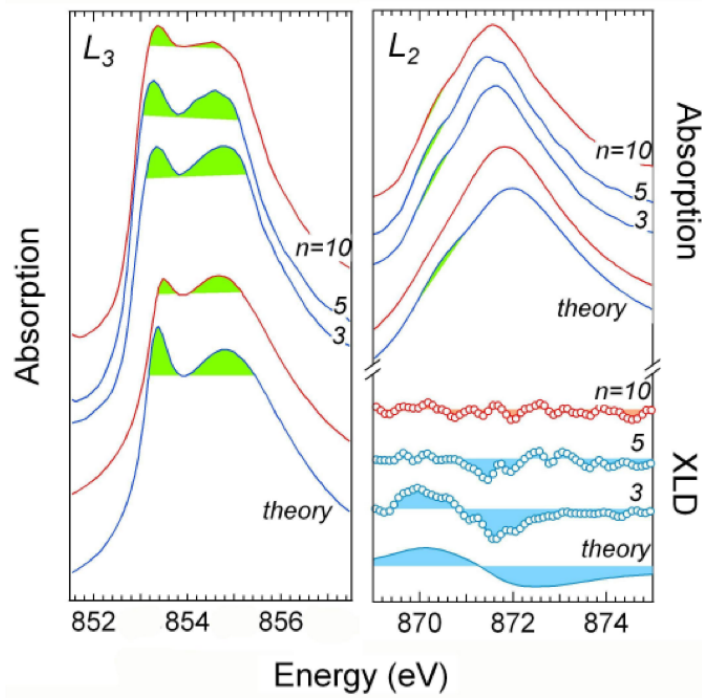


**Figure 5.** X-ray absorption spectra of (LNO) $n$ /(LAO)3 SLs at the L3 (left panel) and L2 (right) edges for  $n = 3, 5$ , and 10 (top). The bottom shows the theoretical calculations done for energy (eV) NiO<sub>6</sub> cluster for a charge-transfer energy of 0.8 (red) and 1.6 (blue) eV. The shaded (green) areas indicate where the most significant changes occur due to the changes in covalency.

To identify the ground states, DC transport measurements from 400 K to 2 K were performed in a commercial physical properties measurement system. The temperature dependent

conductivity,  $\sigma(T)$ , of the SLs is shown in Fig. 6. A transition from metallic to insulating behaviors can be clearly seen with decreasing  $n$ . The  $n$ -dependence of  $\sigma$  (the left inset of Fig. 6) also shows orders of magnitude change across the series. The  $n = 5$  and 10 SLs are metallic at high temperature and reach conductivity maxima,  $\sigma_{\max}$ , at  $T_{\max} = 120$  K and 10 K, respectively. For the  $n = 10$  SL,  $\Delta\sigma(T) (\sigma(T_{\max}) - \sigma(2 \text{ K}))$  is only  $\sim 52.5$  S/cm, relatively small compared with  $\sigma(2 \text{ K})$  ( $\sim 1\%$ ). This  $d\sigma/dT > 0$  region is attributed to quantum correction for metal. In contrast,  $\Delta\sigma(T)$  ( $\sim 381.6$  S/cm) for  $n = 5$  is similar to  $\sigma(2 \text{ K})$  and almost twice of the increase in  $\sigma(T)$  from 400 K to  $T_{\max}$ . This behavior implies the system is on the verge of MIT.

To quantify the transport properties, we fitted the data to various temperature dependent behaviors. The low temperature part of the  $n = 3$  SL is found to be well fitted with the 2D variable range hopping behavior ( $\ln\sigma \propto -T^{-1/3}$ ) up to 20 K. It switches to 3D variable range hopping ( $\ln\sigma \propto -T^{-1/4}$ ) up to around 80 K. The presence of hopping conductivity reveals that the system is on the insulating side of the MIT when  $n = 3$ . On the metallic side, the resistivity of the  $n = 10$  SL,  $\rho$ , follows a  $T$ -linear behavior above 200 K and then enters a crossover region before switching to a  $T^{1.5}$ -dependence below 110 K. The low temperature  $T^{1.5}$ -dependence may be related to proximity to an itinerant to localized transition. Below  $T_{\max}$ , while quantum correction often consists of multiple contributions, fitting with a complete expression is inconclusive due to the limited range of data. Instead, fitting with a simple power-law relation ( $\sigma \propto T^m$ ) yields  $m \approx 1/3$  for data below 5.5 K. It is interesting to note that, while  $m = 1/2$  arising from electron-electron interaction can describe quantum correction in many correlated metals,  $m$  is found to decrease from  $1/2$  to  $1/3$  in a number of metallic perovskite oxides, including LNO, when approaching the MIT from the metallic side upon reducing the carrier density. For the  $n = 5$  SL,  $\rho$  is also linear with temperature above 270 K. The region between that and  $T_{\max}$  appears to be a crossover as no simple power-law dependence is found.

Unlike the  $n = 3$  and 10 SLs, the  $d\sigma/dT > 0$  region of the  $n = 5$  SL cannot be accounted by hopping conductivity or quantum correction. Imposing the  $T^m$  power-law relation gives rise to a strongly temperature-dependent  $m$ , which increases continuously to about 0.9. This interesting behavior is probably related to the fact that  $\Delta\sigma \approx \sigma_0$ , indicating that all the interactions involved

in the dimension-control, such as correlation effects and the bandwidth, are of a similar strength. The  $n = 5$  SL, thus, falls into a critical region of the MIT.

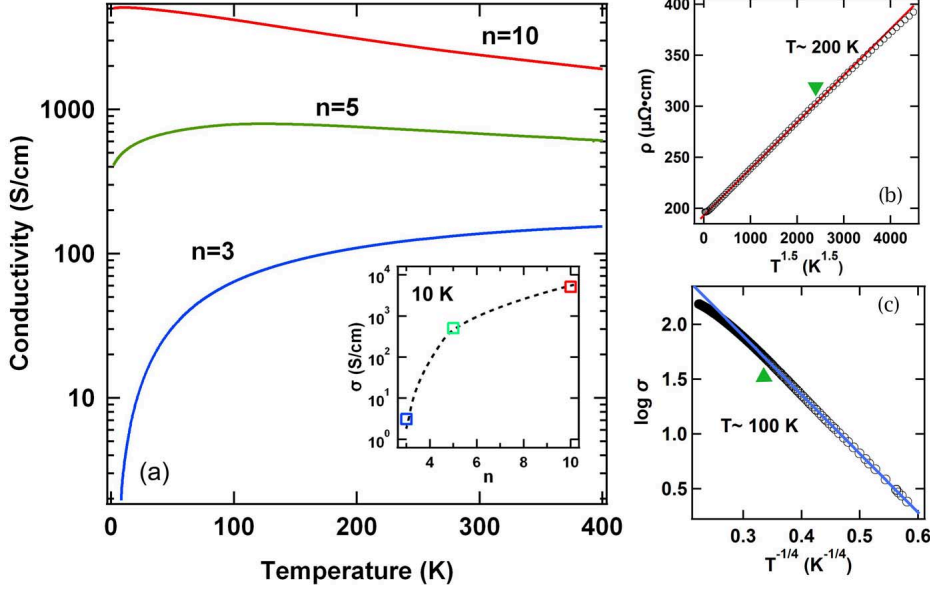


**Figure 6:** (a) Conductivity of  $(\text{LNO})_n/(\text{LAO})_3$  SLs versus temperature. Inset: conductivity versus  $n$  at 10 K. The dashed line is a guide for eye. (b) Resistivity as a function of  $T^{1.5}$  at  $n = 10$ . The red solid line is a guide for eye. (c)  $d \ln \sigma$  as a function of  $1/T^{1/4}$  for the  $n = 3$  SL shows the low temperature three dimensional variable range hopping behavior.

#### 4. RESULTS AND DISCUSSION ON ELECTRONIC PROPERTIES

High-quality epitaxial  $[(\text{LNO})_n/(\text{LAO})_3]_N$  SLs ( $n = 3, 5$  and  $10$  with  $N = 10, 4$  and  $2$  respectively) were grown by laser molecular beam epitaxy (MBE) as described above. +2.2% tensile strain is applied with  $\text{TiO}_2$ -terminated (001)  $\text{SrTiO}_3$  (STO) substrates. To explicate the evolution of the ground state due to quantum confinement, DC transport measurements from 400 K to 2 K were performed by using the *van der Pauw* method. The obtained temperature-dependent conductivity  $\sigma(T)$  of the SL series is shown in Fig. 6(a). A transition from metallic to insulating behavior can be clearly seen with decreasing  $n$ . The inset of Fig. 6(a) also demonstrates orders of magnitude change in  $\sigma$  across the series taken at 10 K. As seen, in analogy to the bulk LNO, the  $n = 10$  SL exhibits a highly metallic behavior ascribed to the three dimensional regime. On the other hand, unlike the bulk, which is known to follow a  $T^{3/2}$  dependence at room temperature and switch to a low-temperature  $T^2$  Fermi liquid behavior, the resistivity  $\rho$  at  $n = 10$  switches from a  $T$ -linear behavior above 200 K to a  $T^{3/2}$  power law (see Fig. 6(b)). Note that, while a  $T$ -linear dependence was also found in the high-temperature metallic phase of other members of the bulk  $\text{RNiO}_3$  family who have a charge-ordered insulating ground state, the low-temperature  $T^{3/2}$  behavior of Fermi liquid electrons has been attributed to

scattering by bond-length fluctuations due to proximity to a Mott-type MI transition from the itinerant side. These phenomena indicate enhanced electronic correlations in the quantum confinement regime and stronger vibronic fluctuations associated with charge ordering.

The intermediate thickness  $n = 5$  SL still shows a clear metallic behavior at high temperatures but reaches a conductivity maximum at  $T_{\text{max}} = 120$  K. While the metallicity of LNO films under large tensile strain is known to cease when the thickness is  $\leq 3$  nm, it is remarkable that the high-temperature metallic behavior is well maintained in such a thin slab ( $< 2$  nm). This result unambiguously highlights the exquisite role of the confinement structure with interfaces in defining the transport properties of SLs as compared to the bulk LNO and single layer films. Notice, the conductivity  $\sigma$  here is also well below the Ioffe-Regel limit ( $\sim 2000$  S/cm), manifesting the modification of the correlation nature of the observed behaviors and the minor role of disorder. Below  $T_{\text{max}}$ ,  $\sigma(T_{\text{max}}) - \sigma(2\text{K})$  ( $\sim 381.6$  S/cm) is as large as  $\sigma(2\text{K})$  and almost twice of  $\sigma(T_{\text{max}}) - \sigma(400\text{ K})$ . Neither hopping conductivity nor quantum corrections is found to be able to account for this  $d\sigma/dT > 0$  region. This transitional behavior explicitly indicates that all the involved interactions and relevant energy scales, like electron correlations and the bandwidth, are of a similar strength and strongly competing with each other. Thus,  $n = 5$  falls into a critical region of the confinement-controlled MIT. Upon further decreasing  $n$  to 3,  $d\sigma/dT > 0$  at all temperatures and a variable range hopping behavior was found below 100 K, indicating that finite density of states remains within the opening gap during the dimensional crossover.

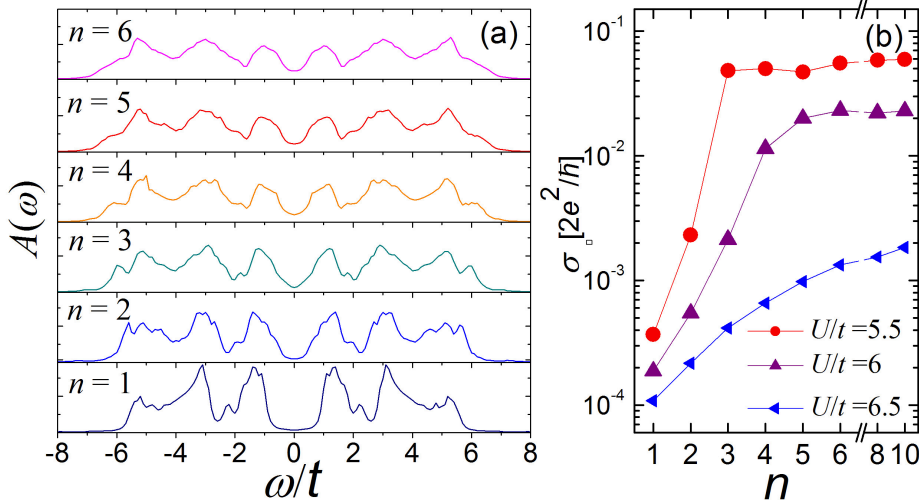


**Figure 7:** Layer CDMFT results for the multilayer Hubbard model with various thickness  $n$ . The transfer anisotropy  $\delta$  is set at 0.2. (a) Average spectral function for  $U/t = 6$ . (b) Sheet conductance  $\sigma$  versus  $n$  for  $U/t = 5.5, 6$  and  $6.5$ .

To elucidate the origin of the MI transition induced by quantum confinement, we compare the dimensional crossover with the layer extension of cellular dynamical-mean-field theory (layer CDMFT) which takes into account the competition between the short-range correlations and the reduced bandwidth. To make the problem tractable and yet relevant for the SLs, we considered the multi-layered single-band Hubbard model for Ni 3d and simulated the high-energy Al 3s

states as vacuum. Note that CDMFT was recently applied to explain the opening of a correlation-induced pseudogap in SrVO<sub>3</sub> thin films. The effective impurity model for each layer consisting of 2×2 plaquette coupled to 8 bath orbitals and is solved by using the Lanczos exact diagonalization method. The layer CDMFT employed here goes beyond that previous study by including short-range correlations within each monolayer to capture the physics of pseudogap. The short-range correlation is antiferromagnetic as recently suggested in a similar system with the planar  $d_{x^2-y^2}$  orbital configuration. To neutralize the CDMFT's overemphasis on the in-plane correlations, we introduce a small anisotropy between the in-plane  $t_{in}$  and out-of-plane  $t_{out}$  hopping integrals as  $t_{in} = t(1 - \delta)$  and  $t_{out} = t(1 + 2\delta)$  so that  $t_{out}$  competes with the in-plane correlations. The bandwidth of the bulk non-interacting system is unchanged,  $W = 12t$ .

Since bulk LNO is a metal we consider moderate values of  $U/t$  ( $U = 6t$ ). Fig. 7(a) presents the  $n$ -dependent evolution of the spectral function. As clearly seen, the correlation gap in the two dimensional limit is filled up and becomes a pseudo-gap with increasing  $n$ , lending theoretical support to the notion that the experimentally observed MI transition arises from the dimensional evolution of a quantum confined correlated carriers transforming from an insulator to a metal through a "bad" metal phase. Notice, the sharp quasiparticle peak is absent at  $\omega = 0$  even in the thickest slab because out-of-plane correlations are treated on a mean-field level. To see the relation between the (pseudo) gap opening and the anomalous transport properties, sheet conductance  $\sigma$  is computed by the standard Kubo formula. An imaginary part  $\eta = 0.1t$  was introduced to the real frequency  $\omega$  to represent the finite impurity scattering. As shown in Fig. 7(b), with increasing  $n$ ,  $\sigma$  increases continuously and becomes practically unchanged above a critical thickness  $n_c$  below which the pseudo-gap is pronounced. These results reproduce well the critical regime at  $n_c \approx 5$  in the transport measurements and strongly suggest the confinement-controlled short-range electron correlations as the origin of the observed MI transition. From the comparison above, we can see that the essential physics of metal-insulator crossover by the quantum confinement is captured by the CDMFT. On the other hand, as discussed earlier, it is known that rare-earth nickelates also have an intrinsic propensity towards the local charge disproportionation upon entering the insulating phase. The result is a complicated 3D ordering of both charge and spin which might emerge as a competing ordering. To gain microscopic insight into the local electronic structure and the effect of confinement on the MI transition, we carried out detailed x-ray absorption spectroscopy (XAS) measurements. All spectra were acquired in the bulk-sensitive fluorescence-yield mode at the Ni  $L$ -edge. The normalized spectra obtained at 300 K (not shown). The La  $M_4$ -edge which partially overlaps with the Ni  $L_3$ -edge was subtracted with a Lorentzian profile. For direct comparison, the  $L$ -edge spectra of bulk LNO and SmNiO<sub>3</sub> are included. As seen, the energy position and the lineshape of the SLs are close to those of the bulk RNiO<sub>3</sub>, indicative of a Ni<sup>III</sup> charge state of the low-spin configuration. On the other hand, while the multiplet effects are smeared in the metallic bulk LNO, the  $L_3$ -edge spectra of the SL show a pronounced two-peak structure (shaded in green), closely resembling the absorption spectrum of the bulk SmNiO<sub>3</sub>, which in the bulk is a well studied case for the charge-ordered ( $2\text{Ni}^{III} \rightarrow \text{Ni}^{II} + \text{Ni}^{IV}$ ) insulating state. As  $n$  decreases this multiplet effect becomes more pronounced, particularly in moving from  $n = 10$  to 5. The energy separation of the two split peaks is also clearly increasing. The corresponding trend at the  $L_2$ -edge emerges as a



developing low-energy shoulder at about 870.5 eV. The observed evolution is reminiscent of that reported for the bulk  $\text{RNiO}_3$  when crossing the MI boundary, unambiguously revealing the carrier localization in the presence of a developing correlated charge gap in the quantum-confined LNO slabs and a latent tendency to CO during the 3D-to-2D crossover. In accordance with the observations from DC transport, the emergence of the multiplet even in the relatively thick LNO slab ( $n = 10$ ) lends solid support to strongly confinement-enhanced correlations. Meanwhile, when subject to this enhancement, the inclination to CO corroborates its role as a primary competing ground state not only in the bulk but also in the predicted heterostructured LNO.

#### **4. EFFECTS OF HETEROEPITAXIAL STRAIN**

Heteroepitaxial strain is one of the most important and most extensively utilized control parameters in epitaxy engineering. It is also an inevitable effect because lattice mismatch always exist between two different materials. As directly acting on the lattice of a thin layer of material by interfacial bonding, epitaxial strain is often more efficient than elastic mechanical stress and the resulting property modifications can be dramatic. Therefore, to rationally design a heterostructure, the lattice mismatch is an essential starting point. In this section, we will discuss how the bi-axial character of heteroepitaxial strain affects the orbital degree of freedom of  $d$ -electrons in  $\text{LaNiO}_3$  (LNO) ultrathin films, since orbital-lattice interaction, e.g. the crystal field effect and the JT effect, is critical to the local electronic configuration and related long-range orderings. The second part will go further to show the control of heteroepitaxial strain on the  $p - d$  covalency via modulating both the self-doping and hybridization. As a result, the metal-insulator (MI) transition and the collective charge- and spin-ordered ground state of  $\text{NdNiO}_3$  (NNO) ultra- thin films can be fine tuned within a larger phase space.

#### **5. ORBITAL RESPONSE TO LATTICE MISMATCH**

Heteroepitaxy is a powerful venue to modify orbital-lattice interactions in correlated materials with strong electron-electron interactions derived from transition metals with open  $d$ -shell configurations. However, efforts to rationally control properties that are exceedingly sensitive to small perturbations through the strong orbital-lattice coupling are impeded by a poor understanding of how the epitaxial interfaces impose constraints on the orbital response. Thus, despite the recent progress in strain-induced orbital engineering, a crucial fundamental question remains: when a single electron occupies a doubly degenerate manifold of  $d$ -orbital in an octahedral crystal field, such as in perovskites with  $\text{Cu}^{2+}$ ,  $\text{Mn}^{3+}$  or low-spin  $\text{Ni}^{3+}$  cations, how do the interface-imposed epitaxial constraints select the correlated orbital response and electronic configurations?

The exceptional strain-control of the frontier atomic orbitals relies on the susceptibility of the orbital occupations and their energy splitting to bi-axial strain-induced lattice deformations. For this reason, the conventional orbital engineering approach in perovskite oxides is often rationalized as follows: heteroepitaxial strain imposes a tetragonal distortion on the film's primitive unit cell, which results in a modification of the M-O bond lengths of the  $\text{MO}_6$  octahedral units. The bond distortions in turn reduced the crystal field symmetry and remove the



two-fold  $e_g$  orbital degeneracy. Since the  $x^2 - y^2$  and  $3z^2 - r^2$  orbitals represent in-plane and out-of-plane electron densities, respectively, it is generally anticipated that tensile and compressive strains should symmetrically split their energy levels but with opposite signs. The bands derived from these two orbitals are either lowered or raised relative to their strain-free band center of mass, leading to an orbital polarization with a finite filling. This symmetric strain-induced orbital polarization (SIOP) concept is routinely used to rationalize the orbital responses of many complex oxide systems, and also plays a key role in several recent theoretical proposals for replicating high- $T_C$  cuprate physics in perovskite nickelate heterostructures. However, the strategy for tuning the correlated ground states in ultra thin films devised from this SIOP concept is violated more often than it applies: for instance, doped manganite thin films exhibit  $3z^2 - r^2$  orbital polarization plainly inconsistent with the SIOP model regardless of whether the applied bi-axial strain is tensile or compressive. Ultra thin cuprate bilayers also show variable critical temperatures depending on the layering sequence correlated with the sign of the interface lattice misfit, and an ferromagnetic order can be switched on (or off) depending on the strain state in otherwise diamagnetic cobaltite films. In this section, we will provide insight into the violation of the SIOP model via our investigation on the orbital-lattice interactions in 10-u.c. thick films of orbitally degenerate ( $e_g^1$ ) LNO.

## 6. RESULTS AND DISCUSSION ON EFFECTS OF STRAIN

Here we focus on the evolution of the orbital polarization under two representative strain states: compressive and tensile strain on  $\text{LaAlO}_3$  (LAO) and  $\text{SrTiO}_3$  (STO) substrates respectively. We synthesized high-quality (001)-oriented 10 unit-cell (u.c.) epitaxial LNO films by laser molecular beam epitaxy (MBE) as described above. Single crystal LAO and STO were used to apply opposite bi-axial strain states; lattice mismatch is  $-1.1\%$  on LAO and  $+1.8\%$  on STO. To probe the response of the Ni  $3d$  orbital occupations, we employed x-ray absorption spectroscopy (XAS) with linearly polarized lights, i.e. x-ray linear dichroism (XLD), at the Ni  $L$ -edge. Figure 8 shows the normalized absorption spectra taken by the fluorescence yield mode at room temperature for in-plane ( $H=E \perp c$ ) and out-of-plane ( $V=E \parallel c$ ) polarizations under the two opposite strain states.

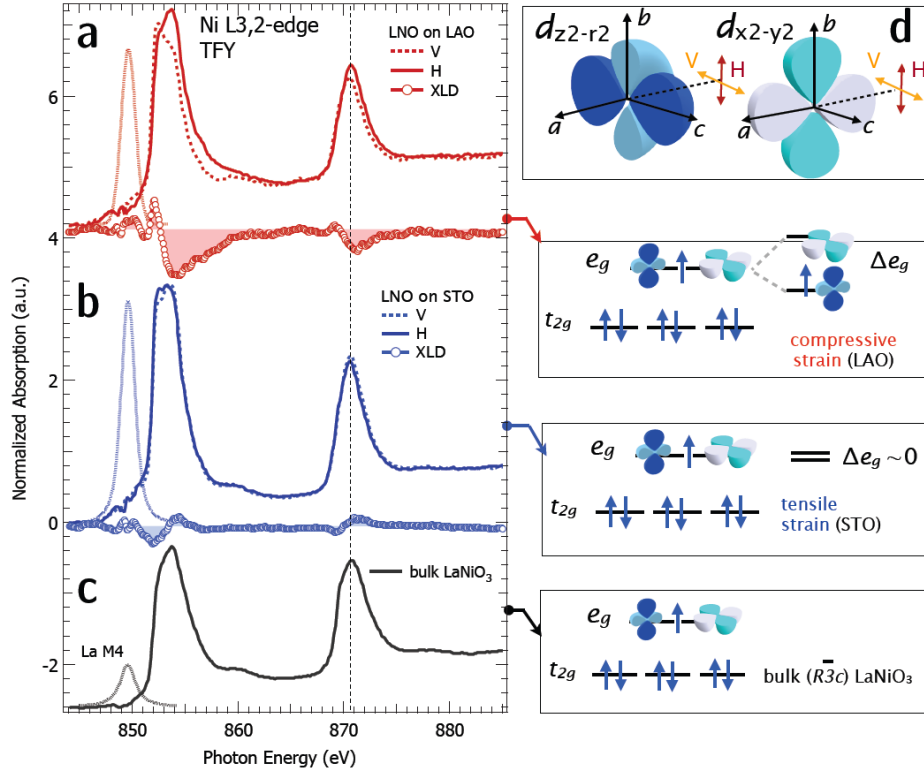


**Figure 8:** Normalized absorption spectra at the NiL-edge taken in the bulk-sensitive fluorescence mode with varying photon polarization (see legend) for films under compressive (red) (a) and tensile (blue) (b) strain, on LAO and STO substrates, respectively. The black curves in (c) represent the bulk (ceramic) LNO data. (RIGHT) Schematic orbital level diagram for bulk LNO and the anticipated strain-induced orbital polarization effect on the  $e_g$  doublet.

As seen, each polarization averaged spectra is representative of octahedrally coordinated  $\text{Ni}^{3+}$  and in good agreement with the spectrum taken on bulk LNO (see Fig.8(c)). There are distinct differences, however, in the polarization dependence between films under compressive and tensile strain. Specifically, as showed in Fig. 8(a), the absorption for the out-of-plane polarization is shifted by  $\sim 100$  meV lower in energy than the in-plane polarization for LNO under compressive strain on LAO. This dichroism indicates a small  $e_g$  band splitting between the Ni-derived  $x^2 - y^2$  and  $3z^2 - r^2$  orbitals due to the distortion of the spherical charge distribution around the Ni sites by non-uniform Ni-O bond lengths. The sign of the XLD implies that the in-plane Ni-O bonds are moderately compressed relative to the out-of-plane apical Ni-O bonds along the  $c$ -axis in agreement with the model of SIOP concept.

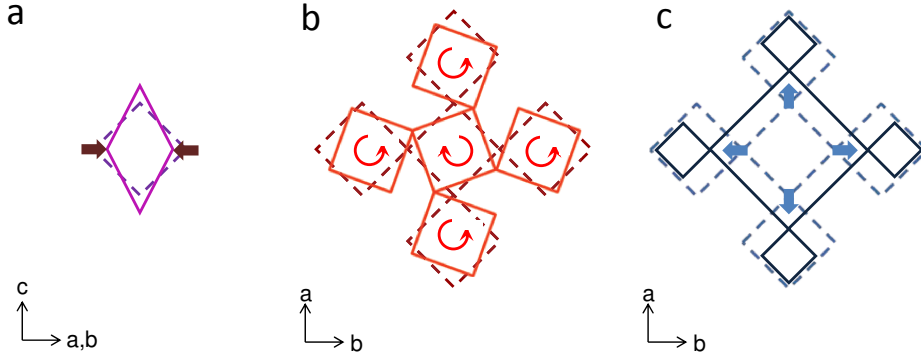


**Figure 9:** Different types of distortions for accommodating lattice mismatch. Dashed diamonds stand for undistorted octahedral network, while the solid ones represent the distorted network. Arrows denote the distortion motions. a) compressed octahedron in accordance with SIOP. b) cooperative octahedral rotation. c) breathing mode.

For tensile strain with the same substrate-film orientation, the SIOP model predicts an inversion of the orbital polarization and the population of the  $d_{x^2-y^2}$  orbital; however, the polarization dependence of our films on STO is remarkably different. As seen, the orbital dichroism is practically absent. This result implies that the uniform Ni-O bond lengths and the highly symmetric crystal field remain seemingly intact despite the large ( $\sim +2\%$ ) tensile strain.

These findings are surprising since, according to the SIOP framework, the larger magnitude of the strain from STO than LAO should also produce a large orbital polarization albeit with an opposite sign. The violation of the SIOP model under the tensile strain demonstrates an asymmetrical orbital response to the bi-axial epitaxial strain, and is indicative of other efficient competing mechanisms in accommodating the lattice mismatch. One possibility is the octahedral rotation which can modulate the pseudocubic lattice parameter by changing the Ni-O-Ni bond angle instead of the Ni-O bond length. Density functional calculations within the local-spin density approximation (LSDA) plus Hubbard  $U$  method were also computed based on our experimentally determined lattice parameters. The resulting structural optimizations are indeed consistent with our findings by XLD. While the structure on LAO consists of a single Ni site with different in-plane and out-of-plane Ni-O bond lengths that lift the formerly bulk-like cubic Ni-site symmetry and the orbital degeneracy, it shows a pronounced pattern of octahedral rotations on STO. Moreover, the tensile strain also stabilizes an additional intriguing breathing mode imposed on the NiO<sub>6</sub> octahedral network to accommodate the lattice mismatch. This ‘breathing’ octahedral distortion induces a Ni-O bond length disproportionation by splitting the equivalent Ni sites into Ni(1) and Ni(2) that are located at the center of nearly ideal NiO<sub>6</sub> octahedra with different average Ni-O bond lengths of 2.00 Å and 1.93 Å, respectively.

## PUBLICATIONS RESULTED FROM THE PROJECT

### Accepted

1. *Epitaxial Stabilization of YNiO<sub>3</sub> Ultra-thin films*, D. Mayers, J. Liu, J. Freeland, B. Gray, E.J. Moon and **J. Chakhalian**, to appear in Journal of Crystal Growth. (2012).

### Published

2. *Whither the oxide interface*, **J. Chakhalian**, A. Millis and J. Rondinelli, *Nature Materials*, 11, 92–94 (2012).
3. *Strain-controlled band engineering and self-doping in ultrathin LaNiO<sub>3</sub> films*, E. J. Moon, J. M. Rondinelli, N. Prasai, B. A. Gray, M. Kareev, **J. Chakhalian**, and J. L. Cohn, *Phys. Rev. B* (Rapid Communications) 85, 121106(R) (2012).
4. *Mott physics near the insulator-to-metal transition in NdNiO<sub>3</sub>*, M.K. Stewart, Jian Liu, M. Kareev, **J. Chakhalian**, and D.N. Basov, *Phys. Rev. Lett.* 107, 176401 (2011).
5. *Orbital control and altered covalency in strained ultra-thin LaNiO<sub>3</sub>/LaAlO<sub>3</sub> superlattices*, J.W. Freeland, Jian Liu, M. Kareev, B. Gray, J.W. Kim, P. Ryan, R. Pentcheva and **J. Chakhalian**, *Europhysics Letters*, v. 96, Issue 5, pp. 57004 (2011).
6. *Asymmetric orbital-lattice interactions in ultra thin complex oxides films*, **J. Chakhalian**, J.M. Rondinelli, Jian Liu, B. Gray, M. Kareev, M. Varela, E.J. Moon, S. Altendorf, F. Strigari, B. Dabrowski, H. Tjeng, P.J. Ryan, and J.W. Freeland, *Phys. Rev. Lett.* 107, 116805 (2011).
7. *Quantum confinement of Mott electrons in ultrathin LaNiO<sub>3</sub>/LaAlO<sub>3</sub> superlattice*, Jian Liu, S. Okamoto, M. van Veenendaal, M. Kareev, B. Gray, P. Ryan, J.W. Freeland, **J. Chakhalian**, *Phys. Rev. B: Rapid Communications* (Editor's suggestion) 83, 161102(R) (2011).
8. *Optical probe of strong correlations in LaNiO<sub>3</sub> thin films*, M.K. Stewart, Jian Liu, R.K. Smith, B.C. Chapler, C.H. Yee, D. Meyers, R.E. Baumbach, M.B. Maple, K. Haule, **J. Chakhalian**, and D.N. Basov, *J. of Appl. Phys.* 110, 033514 (2011).
9. *Optical study of strained ultrathin films of strongly correlated LaNiO<sub>3</sub>*, M.K. Stewart, C.H. Yee, Jian Liu, M. Kareev, R.K. Smith, B.C. Chapler, , K. Haule, M. Varela, P. Ryan, **J. Chakhalian**, and D.N. Basov, *Phys. Rev. B* 83, 075125 (2011).
10. *Sub-monolayer nucleation and growth of complex oxide heterostructures at high supersaturation and rapid flux modulation*, M. Kareev, S. Prosandeev, Jian Liu, B. Gray, P. Ryan, A. Kareev, E.J. Moon, **J. Chakhalian**, *J. of Appl. Phys.* 109, 114303 (2011).
11. *Strain dependent transport properties of the quasi two-dimensional correlated metal LaNiO<sub>3</sub>*, E.J. Moon, B.A. Gray, M. Kareev, Jian Liu, S.G. Altendorf, F. Strigari, L.H. Tjeng, J.W. Freeland, **J. Chakhalian**, *New J. of Phys.* 13, 073037 (2011).

12. *Strain-mediated metal-insulator transition in epitaxial ultra-thin films of NdNiO<sub>3</sub>*, Jian Liu, M. Kareev, B. Gray, J.W. Kim, P. Ryan, B. Dabrowski, J.W. Freeland, and **J. Chakhalian**, *Appl. Phys. Lett.* 96, 233110 (2010).
13. *Effect of polar discontinuity on the growth of LaNiO<sub>3</sub>/LaAlO<sub>3</sub> superlattices*, Jian Liu, M. Kareev, S. Prosandeev, B. Gray, P. Ryan, J.W. Freeland, and **J. Chakhalian**, *Appl. Phys. Lett.* 96, 133111 (2010).
14. *Visualizing nanoscale electronic properties at a complex oxide interface*, T.Y. Chien, Jian Liu, **J. Chakhalian**, N. Guisinger, J.W. Freeland, *Phys. Rev. B: Rapid Communications* (Editor's suggestion) 82, 041101(R) (2010).
15. *Depth-resolved subsurface defects in chemically etched SrTiO<sub>3</sub>*, Jun Zhang, D. Dou, T. Merz, **J. Chakhalian**, M. Kareev, Jian Liu, and L.J. Brillson, *Appl. Phys. Lett.* 94, 092904 (2009).
16. *Atomic control and characterization of surface defect states of TiO<sub>2</sub> terminated SrTiO<sub>3</sub> single crystals*, M. Kareev, S. Prosandeev, Jian Liu, C. Gan, A. Kareev, J. W. Freeland, Min Xiao, and **J. Chakhalian**, *Appl. Phys. Lett.* 93, 061909 (2008).